Interpretable neural network predictions of high-intensity femtosecond x-ray free-electron laser pulses using sulfur K-shell emission spectra

Harald Agelii,[1] Alfredo Bellisario,[1] Carl Caleman,[1,2] Nicusor Timneanu,[1,*] and Sebastian Cardoch[1,†]
[1]*Department of Physics and Astronomy, Uppsala University, Box 516, 75120 Uppsala, Sweden*
[2]*Center for Free-Electron Laser Science CFEL, Deutsches-Elektronen Synchrotron DESY, Notkestr. 85, 22607 Hamburg, Germany*

(Received 8 March 2025; accepted 23 June 2025; published 17 July 2025)

The emergence of high-intensity femtosecond duration x-rays from Free-Electron Lasers has enriched our understanding of the structure and dynamics of biological molecules at the atomic level. In serial femtosecond crystallography experiments, the magnitude of the interaction between photons and matter can vary significantly due to variations in the x-ray pulse's intensity, energy bandwidth and duration, as well as fluctuations in the synchronicity between the x-ray pulse and the sample. Accurate characterization of the conditions from each exposure is valuable for experiment and theory. In this theoretical work, we propose using x-ray emission spectra emanating from sulfur atoms, which are prevalent in biomolecules, to obtain individual hit information. We train a neural network based on synthetic K-shell emission spectra from a lysozyme crystal to predict x-ray fluence and pulse duration. The model achieves a training relative error of $<12\%$ when predicting both parameters concurrently. We use interpretation methods to identify the regions in the spectra that have the most predictive power. For fluence predictions, the model emphasizes K-L emission shifts to higher energies due to the presence of highly charged sulfur ions. For pulse duration predictions, the model places a greater focus on the emission signal from double core hole K-L emission. These results demonstrate that it is possible to predict x-ray exposure information on the sample based on physically interpretable features in sulfur's K-shell emission spectra.

DOI: 10.1103/dwc6-7hvn

I. INTRODUCTION

Serial Femtosecond x-ray (SFX) crystallography using x-ray Free-Electron Lasers (XFELs) offers a way to obtain atomic structural information and dynamics from biological samples at room temperature [1,2]. The high peak brilliance from FELs combined with micron- to nano-sized focusing produces pulses with fluence values in the range of 10^3–10^5 J cm^{-2} that last from a few to tens of femtoseconds [3]. SFX experiments record elastically scattered signals typically from single protein crystals $5-20\,\mu$m in size [4,5] at photon energies in the hard x-ray regimes $\geqslant 5$ keV to achieve high structural resolution [6]. A standard FEL operation mode relies on the self-amplified spontaneous emission (SASE) scheme [7]. The stochastic nature of the SASE process causes shot-to-shot variations in the photon energy, peak fluence, and pulse duration [3]. Knowledge of the temporal-spatial distribution and energy spectrum of the x-ray beam, known as beam characterization, is necessary to have accurate information on the conditions at the interaction region for real-time monitoring and theoretical modeling.

Pulse intensity monitoring happens upstream from the interaction region with x-ray gas monitors [8,9] or solid-state devices [10,11] that do not consider transmission losses through the focusing optics. Even when accounting for transmission [12], there is uncertainty about the proportion of photons that end up diffusely scattered outside the focus. The spatial beam profile can be mapped by fitting a histogram of the total scattered intensities after an experiment [13] or in a separate experiment via charge distributions with volume integration [14]. In liquid or aerosol injection devices, and for crystals (or atomic clusters) that are smaller than or comparable to the focus, there is additional uncertainty about the x-ray exposure at the individual hit level, which depends on the sample position at the moment of illumination [15,16]. As XFEL facilities strive for higher intensities with subfemtosecond pulse durations [17], nonlinear effects that influence the number of photons reaching the detector become increasingly important [18,19]. A present challenge is to have high-repetition diagnostics tools that can provide real-time feedback on experiments [20]. To this end, machine learning approaches have been employed to monitor x-ray pulse properties [21–26] and to characterize samples [27,28].

X-ray emission spectroscopy (XES) is an element-specific and electronic-state sensitive technique that can provide additional complementary information during SFX experiments. XES originating from proteins has been used to study local structures [29]. For example, using a single pulse for SFX and XES, hit rates and oxidation state in the metal active site for metalloproteins have been explored [30]. The low fluorescence photon count from each shot requires high

*Contact author: nicusor.timneanu@physics.uu.se
†Contact author: sebastian.cardoch@physics.uu.se

repetition rates and thousands of shot averages [30]. For light elements, the most probable decay process following inner-shell photoionization is the ejection of a secondary electron. A challenge with using proteins without metallic clusters is their weak fluorescing signal. For example, the possibility to detect a sufficiently strong single-shot sulfur Kα XES signal from ammonium sulfate was experimentally demonstrated in the tender x-ray region using a spectrometer placed at a backscattering angle [31]. Due to the high intensity of x-rays from FELs, a fully exposed sample within femtoseconds turns into a plasma. In the context of laboratory and astrophysical plasma, XES is routinely used to obtain information about the sample's relative composition, temperature, and ionization [32,33].

In this study, we explore the feasibility of obtaining real-time shot-to-shot x-ray pulse characteristics from the XES signal emanating from a protein crystal, which encodes information on the ionization, temperature, and electronic occupations. We train a deep neural network with emission spectra as input to predict one or a combination of fluence and duration from the incident x-ray pulse as output. We compute time-integrated XES using collisional radiative simulations together with fully relativistic configuration averaged atomic data. We apply explainable neural network techniques [34] to identify key spectral features that meaningfully influence the predictions. We see this study as a first step toward developing an x-ray pulse and sample diagnostic tool for SFX and Single-Particle Imaging that is complementary to existing methods.

II. METHODS

A. Simulating emission spectra

When a protein crystal or any material in general is exposed to high-intensity x-rays, radiation damage initiated by inner-shell photoionization starts taking place, resulting in the formation of ions in highly excited states. Within femtoseconds after exposure, radiative and nonradiative relaxation channels along with primary photoelectrons, with a mean free path smaller than the crystal dimensions, trigger a secondary ionization cascade, and the sample reaches a transient nonequilibrium plasma state [35–37]. To describe the sample's changing electronic configuration and energetics initiated by the x-ray pulse, we employ a nonlocal thermodynamic equilibrium collisional radiative code [38,39]. The collisional radiative simulations solve a set of differential equations given an incident x-ray beam photon energy, fluence, bandwidth, and temporal shape. A rate matrix evolves electronic occupations based on radiative and collisional rates specified by the atomic data. Heating rates are used to calculate free-electron and ion temperatures, where each follows a Maxwellian distribution. Electronic occupations dictate opacities and emissivities used for radiation transport. For each simulation time step, the existing conditions are determined iteratively until electronic densities and temperatures converge. The code has been featured in a series of workshops that benchmark and compare collisional radiative codes with experimental spectroscopic data [40]. In the context of biomolecular modeling, this tool has been employed to reproduce experimental observations in x-ray-induced electronic and structural changes [41–43].

TABLE I. Comparing values from the Flexible Atomic Code (FAC) [44] to experimental data. The calculated energies are averaged over fine-structure multiplets for K-L and averaged over all transitions for K-M, where the standard deviation represents their uncertainty. The two experimental values for K-$M_{2,3}$ outline a two-peak substructure identified by Pérez *et al.* [57].

Transition	FAC (eV)	Experimental (eV)	Ref.
K-L_2	2307.07(54)	2306.700(38)	[54]
K-L_3	2307.94(23)	2307.885(34)	[54]
K-$M_{2,3}$	2469.23(27)	2464.49(6)	[57]
		2467.73(2)	

As part of our approach, we use the flexible atomic code (FAC) [44] to compute atomic data for photoionization and radiative recombination, photoexcitation and spontaneous decay, autoionization and dielectronic recombination, electron impact ionization and three-body recombination, as well as electron impact excitation and deexcitation. Inverse processes are determined by the collisional radiative code based on the assumption of statistical equilibrium [45]. FAC solves a relativistic Dirac equation with a central potential with effects from nuclear charge and electron-electron interactions [44]. We get energy levels and degeneracies from the diagonalized Hamiltonian. Radiative electric and magnetic dipole transitions are described by wavelength, oscillator strength, and level width [44]. Electron impact ionization rates are computed over a grid with a limited energy range based on the distorted wave method and fit these to a function that depends on collision impact energies. Since electron impact excitations are especially computationally demanding in FAC, we instead calculate these based on the Bethe approximation using oscillator strengths from photoexcitation [46].

We describe the x-ray pulse with a Gaussian profile in the time domain and a flat top shape in the energy domain. We discuss limitations of these two assumptions in Sec. III. The sample is simulated as a one-dimensional uniform medium with a defined mass density and stoichiometric ratio. For this study, we use a density of 1.13 g/ cm^3 and stoichiometry of $H_{562}C_{187}N_{59}O_{190}S_3$, which was determined from a solvated and equilibrated lysozyme crystal after executing minimization and equilibration molecular dynamics procedures. We define the sample as a one-dimensional 1-μm-thick system with an initial electron and ion temperature of 0.025 eV. The collisional radiative simulations ran for 1 ps. In addition, we incorporate effects from cooling via hydrodynamic expansion and ionization potential depression using the Steward-Pyatt model [47]. We compute configuration-averaged atomic data for $n \leqslant 3, l \leqslant 2$ quantum numbers with a maximum of up to two excitations per n shell from the ground-state configuration. In Table I, we compare energies for a few selected transitions obtained from atomic calculations and experiments. In the time-integrated spectra, we omit contributions from bound-free and free-free emissions. The simulated emission spectra span the emission energy range 2.20–2.51 keV, which covers K-L and K-M shell emission from single 1s core

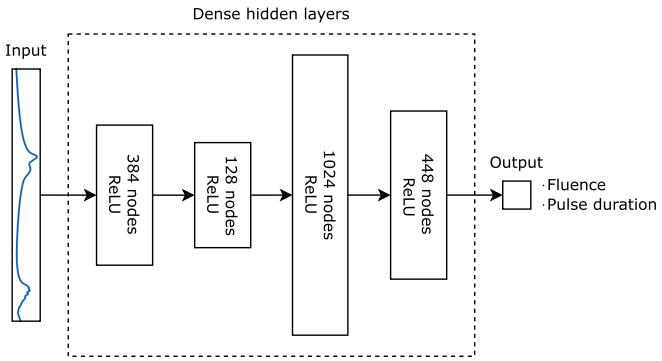

FIG. 1. Fully connected neural network architecture with four hidden layers. Each data point in the processed time-integrated synthetic spectra is fed as an input. The number of outputs is one or a combination of x-ray fluence and pulse duration. We use a linear activation for the output layer.

hole and K-L emission from double $1s$ core hole states. The spectra consist of 340 nonuniformly sampled points that vary between 0.4 and 0.6 eV in regions with emission peaks, and 1.4–4.5 eV in regions without emission peaks.

B. Data processing

Depending on the sample conditions, the wings from bound-bound transitions may introduce an overall shift in the simulated spectra. Although physical, these shifts might not be well captured in an experimental setting due to their generally weak signal. In the early attempts of our study, we found that the neural network model partially learned from these background shifts. Furthermore, experimental emission spectra are commonly given in arbitrary units, where absolute values can be recovered after careful calibration procedures. If real-time knowledge of the sample conditions is desired during an experiment, then accurate calibration might not always be feasible. Motivated by these details, we (1) linearly interpolate the spectra to obtain a uniformly sampled 1000-points-long signal to make sure each input node in the neural network receives the intensity corresponding to the same emission energy value across all spectra; (2) apply a min-max normalization to each emission spectra intensity I_i according to $I_i' = [I_i - \min(I_i)]/[\max(I_i) - \min(I_i)]$ to decouple the magnitude of the x-ray pulse intensity from the emission intensity; (3) augment the data sixfold by introducing a normally distributed random shift centered at zero with a standard deviation of 10% to increase our input data (number of spectra) and remove any fluence dependence on the location of the baseline; and (4) add noise to each spectrum from a normal distribution centered around zero and 0.1% standard deviation.

C. Neural network structure and model interpretation

We construct a fully connected feedforward neural network consisting of four hidden layers with 384, 128, 1024, and 448 nodes, respectively, using the *Keras* PYTHON library [48]. A diagram of the architecture is shown in Fig. 1. We find an optimal number of layers and nodes from a limited set of combinations that minimizes the validation error using the *KerasTuner* PYTHON package [49]. The hidden layers use a ReLU activation function, while the output layer uses a linear activation. The simulated data is split into 80% training and 20% testing partitions. The ground truth training output is scaled from 0 to 1 using a min-max normalization. We evaluate the accuracy of our predictions during training with a tenfold cross-validation technique. The training data is divided into ten partitions and ten identical independent models are trained on a different combination of partitions with a single partition singled out for validation. We use a mean squared error loss function, a batch size of 16, and train for 500 epochs. The models are optimized using the Adam optimizer and a dynamic learning rate 1×10^{-3} to 1×10^{-5} that decreases by a factor of 0.9 when the validation loss stagnates for 10 epochs.

After training, we gain an interpretation of the results by computing one-dimensional saliency maps with two techniques. (1) We use the GradientTape interface implemented in the *TensorFlow* PYTHON library [50] to measure the sensitivity of the model based on the gradient of its output with respect to the input. (2) We compute approximate Shapley Additive Explanations (SHAP) values, using the Deep Learning Important FeaTures [51] method implemented in the *shap* PYTHON library [52]. SHAP is a gradient-free method that compares neuron activation differences between reference and test inputs to assign importance scores. As a reference, we use a set of 100 background noisy spectra containing no information, which we construct from a normal distribution centered around -5 and standard deviation of 10^{-3}.

III. RESULTS AND DISCUSSION

The method of XES is routinely used to probe the local environment of the emitters. The computed data from which we obtain spectral information are atomistic and do not carry any molecular information. We can specify initial oxidation states in the simulations. To keep the results general, we assume all atoms start in a neutral configuration. Following the creation of a $1s$ core hole, the strongest sulfur emission lines, corresponding to a radiative electron decay from the L shell to fill the hole in the K shell, do not significantly shift in energy with oxidation state [53]. K-L emission lines are also less sensitive to chemical bonds compared to K-M shell transitions. The K edge in sulfur at 2470.5 eV [54] does shift to higher energies with increasing charge. For photon energies in the hard x-ray regime, these shifts ($\sim$10 eV from S^{0+} to S^{6+} [53]) are comparatively small and do not significantly alter ionization pathways.

A. Predicting x-ray pulse fluence

We begin by training a model to predict the fluence in the sample. The dataset consists of 6000 time-integrated K-shell sulfur emission spectra. For the generation of the synthetic data, we uniformly sample the fluence range 5×10^3 to 5×10^5 J cm^{-2} using a scrambled Sobol sequence to obtain an even sampling of the fluence (low discrepancy), and fix the pulse duration to 10 fs, the photon energy to 12 keV, and the bandwidth to 1%. A randomly selected spectrum before data processing is shown in Fig. 2(a). We identify

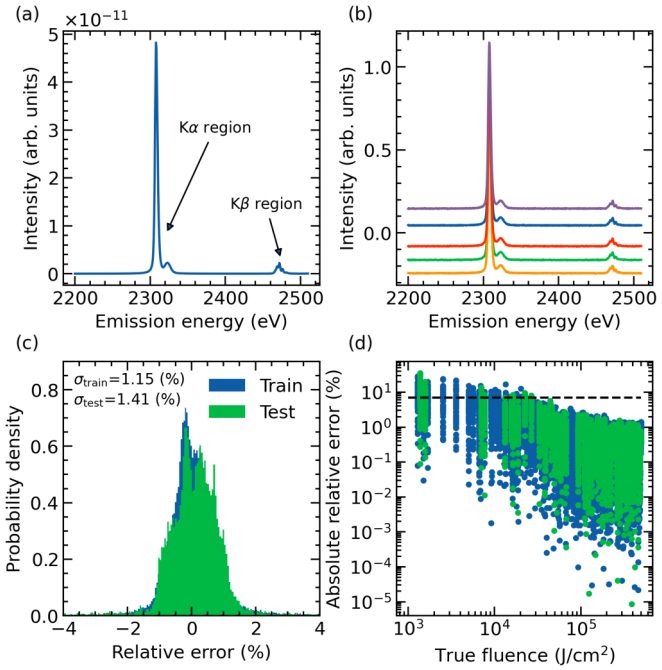

FIG. 2. Training a model based on simulated time-integrated sulfur XES collected for 1 ps to predict fluence on the sample from an incident x-ray Gaussian-shaped 10 fs, 12 keV, and 1% bandwidth pulse. (a) *K*-shell sulfur emission for a single selected run. (b) Augmented data based on the procedure outlined in Sec. II B. (c) Relative mean squared error distribution after tenfold cross validation. (d) Absolute relative mean square error as a function of the true x-ray pulse fluence. The dashed line delineates five times the standard deviation of the relative error from the test set.

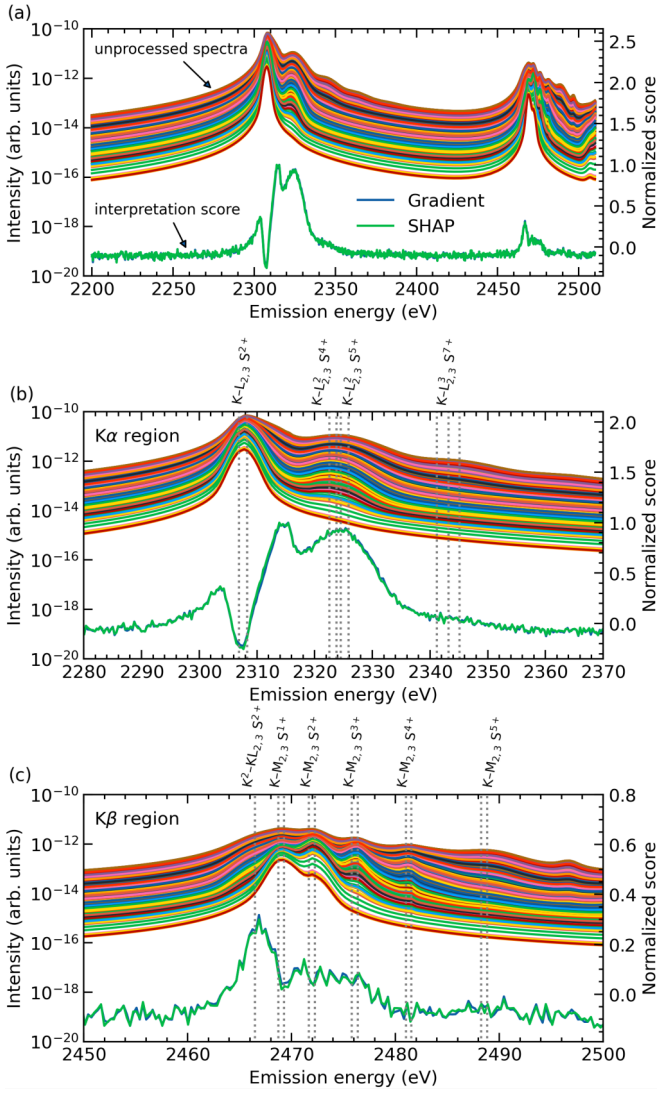

FIG. 3. Gaining interpretation of the trained models by superimposing the unprocessed emission spectra (*y* axis on the left-hand side), together with the normalized interpretation scores obtained from Gradient and SHAP methods (*y* axis on the right-hand side). Panel (a) shows the entire spectral region, while (b) and (c) focus on the Kα and Kβ emission regions, respectively. The interpretation scores are averaged over the fold cross-validation model ensemble. For SHAP, we use a normally distributed noise centered at -5 with a standard deviation of 10^{-3} as the reference. The dotted lines show the identified emission lines that contribute to the main spectral features.

two regions of interest: one around 2.3 keV that we label as Kα and a second around 2.46 keV that we label Kβ. The result from augmenting this single spectrum, based on the procedure described in Sec. II B, is shown in Fig. 2(b). After *n*-fold cross validation using the procedure outlined in Sec. II C, we evaluate the model ensemble on the test dataset. A histogram of the relative error shown in Fig. 2(c) demonstrates the ensemble predictions follow a roughly uniform distribution with a standard deviation of 1.41%. For reference, x-ray gas monitors at the European XFEL have an absolute accuracy of less than 10% [8]. The absolute relative error as a function of the fluence, plotted in Fig. 2(d), shows the model struggles to predict lower fluence values. There are two explanations for this. (1) Low fluence values are significantly smaller than the dataset's average, therefore, a small deviation from their true values constitutes a large relative error. (2) We have fewer simulated spectra at low fluence since we opt to sample the fluence space linearly. We trained additional models using *n*-fold cross validation with a subset of the data corresponding to x-ray fluence values $\leqslant 5 \times 10^4$ J cm^{-2}. We find (results not shown) that the uncertainty in the training's relative error improves slightly compared to evaluating the subset using the full-dataset trained models. Hence, the high fluence bias on the training data affects the model's performance. A uniform distribution of the emission on a logarithmic scale could improve the results.

We would like to gain insights into the features from the input spectra that govern fluence predictions. We employ the methods of Gradients and SHAP discussed in Sec. II C. The normalized interpretation scores from these methods, along with the log-scaled unprocessed spectra, are shown in Fig. 3(a) over the full simulated spectral range. These interpretation scores can be taken as a measure of the interest captured by the model. A positive saliency value corresponds to areas of the spectra containing information that increases the model's confidence, while negative values decrease the model's confidence in its prediction [55]. The absolute value of the saliency therefore highlights the regions of importance

since they impact the model's final prediction [55]. We observe both methods yield very similar scores, with most focus placed around 2.29–2.35 keV. By normalizing the data, the model is unable to correlate the height of the most intense emission peak with fluence. By shifting the data uniformly along the y axis, the model also learns to ignore any background that, due to its relatively weak signal, might be absent in an experiment.

In Figs. 3(b) and 3(c), we zoom into the Kα and Kβ emission regions, respectively, and label selected emission lines following IUPAC notation [56]. The K-$L_{2,3}$ lines, also known as Kα_1 and Kα_2, correspond to $2p \rightarrow 1s$ transitions that under the conditions explored in this study merge into a single peak. With increasing incident fluence, this peak broadens most strongly towards higher energies. The interpretation score around this transition drops at the peak and asymmetrically favors higher energies. This observation aligns with our physical understanding, as the fluence determines the sample's ionization, causing the emission to shift to higher energies. The model also strongly associates fluence prediction with the presence of K-$L^2_{2,3}$ S^{4+} and S^{5+} lines, corresponding to a $2p \rightarrow 1s$ transition with a spectator hole in the L shell [57]. We can also connect this observation with a fluence-dependent sequential multiphoton absorption [35,58–60], where the increasing number of photons can further ionize L-shell electrons from ions in excited or ground-state configurations. Another mechanism to create L-shell spectator holes is via electron impact ionization [57]. At higher fluence values, the sample is more ionized, resulting in an increased number of free electrons available for collisions. To keep the simulations computationally feasible, each charge state contains a limited number of levels, which includes at most two excitations per n shell from the ground-state configuration. Therefore, for weakly ionized ions, emission lines with two or more L-shell spectators are absent in the synthetic spectra but may be present in experimental observations. The signal from higher ionization states, for example, the K-$L^3_{2,3}$ S^{7+} line, corresponding to a $2p \rightarrow 1s$ transition with two spectator holes, does not contribute to the fluence prediction. In the Kβ region, we observe emission from K^2-$KL_{2,3}$ S^{2+}, corresponding to a double core hole $2p \rightarrow 1s$ transition, and from a single core hole K-$M_{2,3}$ at different charge states. In this region, only the lowest energy emission contributes to the fluence prediction.

To further evaluate the model sensitivity to different regions of the spectra, we train a new model on data with some missing information. With this perturbation analysis, we gain knowledge of the emission energy regions that are most important for the prediction [34] and mimic an experimental scenario where the spectral signal might be partially unavailable. In this case, we augment the 6000 spectra dataset twofold. Twenty percent of the spectral emission energy is masked by setting values to zero. The masking is uniformly distributed along the full emission energy range. We train the model on the occluded spectra using n-fold cross validation. The ensemble's mean (dots) and standard deviation (error bars) prediction from the test dataset is presented in Fig. 4. The results show ensemble uncertainties are small in most cases except for a few predictions that fall well outside the general trend. We show the spectra from selected outliers in the inset and identify these happen when prominent Kα and Kβ features of the spectra are fully removed. These results are in line with our previous observation obtained with the methods of Gradient and SHAP. Our results underscore that even with incomplete experimental data, the model maintains robust performance.

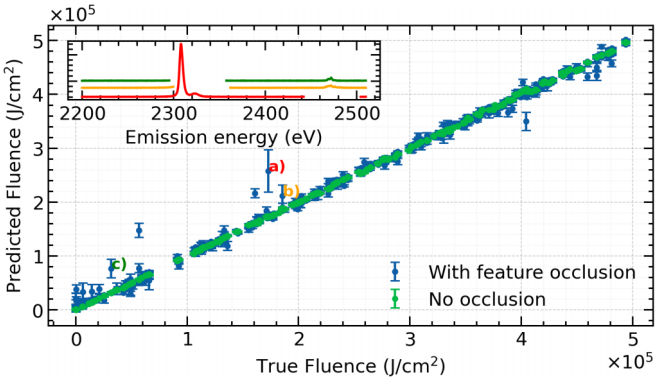

FIG. 4. Comparing ensemble predictions against fluence with and without feature occlusion. At low fluence, the relative uncertainty is higher, but the most significant effect on uncertainty is seen in predictions where the Kα and Kβ regions are occluded, as shown in the inset. We show a few cases corresponding to each labeled prediction, with color-coded letters matching the color of the spectra in the main figure's inset.

B. Predicting x-ray pulse intensity

We examine a more challenging but realistic condition by training models to concurrently predict x-ray fluence and pulse duration. We sample both parameters uniformly in linear scale using a scrambled Sobol sequence in the range 5×10^2 to 5×10^5 J cm^{-2} and 3–30 fs. The dataset consists of approximately 21 000 emission spectra. The incident x-ray photon energy is constant at 12 keV with 1% bandwidth. In Figs. 5(a) and 5(b), we present the absolute relative error obtained from the tenfold cross-validation ensemble. We find a standard deviation of 11.8% and 9.4% for fluence and pulse duration test predictions, respectively. Compared to the model ensemble with fixed pulse duration, the fluence absolute relative error is now much larger. In Fig. 5(c), we compare the true values from the testing dataset (green dots) to the average from the ensemble prediction (yellow lines). In this representation, the results demonstrate the model does well to predict most pulse duration and fluence samples struggling mainly for small fluence values. As we previously determined, this is a consequence of poor sampling of the low fluence region. Nevertheless, the intensity from each exposure shown in Fig. 5(c), based on the predicted fluence over the predicted pulse duration, is decently captured even at low intensities where, for values $\leqslant 1 \times 10^{18}$ W cm^{-2} consisting of only 26 testing samples, the model achieves a 28% standard deviation from the true values.

Similar to the previous section, we are interested in identifying spectral features that are critical to the model's prediction. On this occasion, we focus only on normalized SHAP interpretation scores, presented in Fig. 6(a) over the

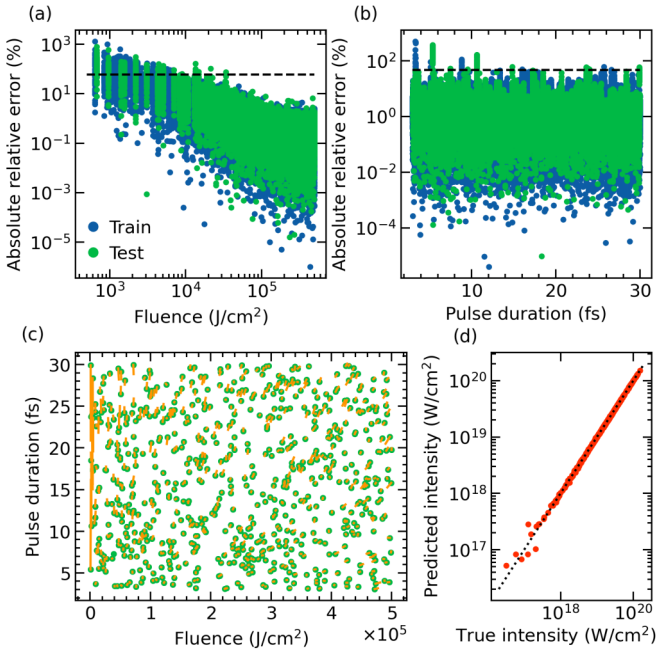

FIG. 5. Model predicting x-ray pulse fluence and pulse duration. (a) Relative error as a function of the fluence and (b) pulse duration. In both panels, the dashed lines represent five times the standard deviation of the relative error from the test set. (c) Comparing the testing dataset's true (green dots) and predicted (yellow lines) values along the two output dimensions. Predictions are averaged over the tenfold cross-validation models. (d) Predicted and true training intensities (fluence over pulse duration). The dotted line delineates a perfect prediction.

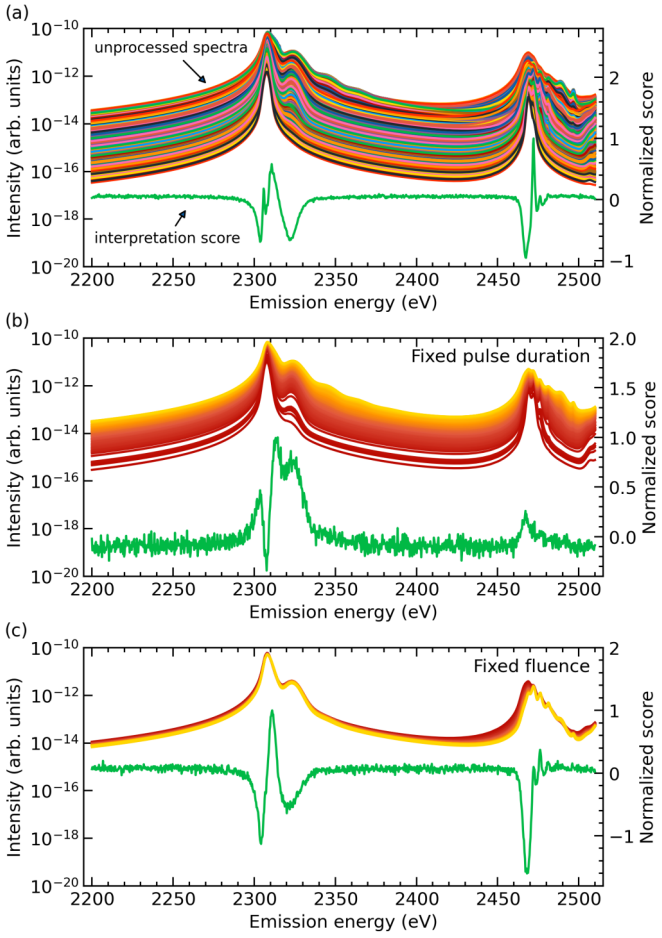

FIG. 6. Gaining interpretation by plotting the unprocessed emission spectra (y axis on the left-hand side) together with the normalized SHAP interpretation score (y axis on the right-hand side). The models are trained to predict (a) both x-ray fluence and pulse duration, (b) only x-ray fluence, with a fixed pulse duration of 8 fs ±5%, and (c) only x-ray pulse duration, with a fixed fluence of 2×10^5 J/cm^2 ±5%. In panel (b), emission lines are colored and sorted by low (red) to high (yellow) incident fluence. In panel (c), emission lines are color sorted by short (red) and long (yellow) pulse durations. The approximate SHAP values are averaged over the tenfold cross-validation model ensemble using a background reference signal constructed from normally distributed noise centered at −5 with a standard deviation of 10^{-3}.

full simulated energy range along with log-scaled unprocessed emission spectra. We compare these results against the interpretation scores presented in the previous section. While the normalized score remains zero for most of the spectra except the Kα and Kβ regions, its overall shape changes and shows a larger emphasis near the Kβ region. We approximately decouple the fluence and pulse duration contribution to the interpretation scores by training two independent n-fold cross-validation model ensembles with a subset of the training data where one parameter is fixed at a time. For fluence and pulse duration, we fix the values to 2×10^5 J/cm^2 and 8 fs, respectively, with an interval of ±5%. The normalized SHAP interpretation scores are shown in Fig. 6(b) for varying fluence and fixed pulse duration and in Fig. 6(c) for varying pulse duration and fixed fluence. When the pulse duration is fixed, we recover similar results to those presented in Fig. 3(a). When the fluence is fixed, the K^2-KL$_{2,3}$ emission responds most strongly to changes in pulse duration and the normalized interpretation score highlights this region as significant for the prediction. The variation in the strength of K^2-KL$_{2,3}$ emission line to pulse duration can be understood by considering sulfur's 1s core hole lifetime is 1.1 fs [61]. As the pulse duration decreases, incoming photons outrun radiative and nonradiative relaxation mechanisms, leading to the creation of empty cores whose presence we detect via this emission channel [62,63]. These observations demonstrate we can train a model to predict x-ray pulse conditions that connect to relevant physical features.

Finally, we discuss our assumption of a flattop pulse shape in the energy domain and a Gaussian shape in the time domain to model x-rays. The bandwidth of a typical SASE pulse is on the order of 1×10^{-3} [7], corresponding to ∼12 eV for a central photon energy of 12 keV. Błachucki *et al.* [64] reported shot-to-shot fluctuations around 50 eV. Given the photon energy in this investigation well exceeds the ionization threshold, we do not expect these variations to modify the sample's XES signal strength. Regarding the temporal structure, we carried out simulations that demonstrated a Gaussian-shaped pulse with identical fluence adequately reproduces time-integrated emission spectra from a SASE pulse shape (results not shown). Rohringer and Santra [65] demonstrated double core hole formation to be sensitive to the

chaotic structure of the FEL pulse. In line with this, we find the highest discrepancy between the two pulse shapes around the K^2-$KM_{2,3}$ emission line with a maximum difference in total emission in the Kβ region of roughly 15%.

IV. CONCLUSIONS

In this study, we propose a neural network method to obtain real-time shot-to-shot x-ray pulse information on the sample based on K-shell emission from sulfur atoms, which are readily found in proteins. To test this method, we train a fully connected neural network on synthetic emission spectra computed with a collisional radiative code. We find an accurate prediction of the fluence with normally distributed relative errors with a standard deviation $\leqslant$1.5%. We also train a model to concurrently predict both fluence and pulse duration and achieve errors with a standard deviation below 12%. We identify spectral features with importance scores obtained from three different interpretation methods (Gradient, SHAPS, feature occlusion), which we link to different physically motivated electronic mechanisms that emerge due to variations in the fluence and pulse duration of the incident x-ray. This is a step towards including explainable artificial intelligence to explain physical phenomena [34].

In this work, we assume a spatially uniform illumination, which holds in the limit of a small crystal compared to the beam's focus. If the crystal is larger or comparable to the beam's focus, this assumption breaks down. A follow-up study could focus on integrated emission spectra from varying incident x-ray intensities to mimic spatial variations. Low fluorescent yield from micron- to nano-sized crystals will pose restrictions on the achievable signal-to-noise ratio. At present, we have assumed a dynamic range of 3 orders of magnitude from each emission spectrum. In an experimental setting, a boost in x-ray emission signal could be initially mitigated by working with clusters of heavy atoms, metalloproteins, or crystals with heavy atoms [5]. A theoretical continuation of this study, which requires a more expansive training dataset, could focus on predicting sample stoichiometry and density information, considering the stochastic temporal structure of the x-ray pulse, as well as handling low signal-to-noise conditions. The accuracy of the atomic model for the validity of the results is important. The energies from atomic calculations are most accurate for highly charged states. For low charge states, these can nonsystematically differ by $\sim$1 eV. Emission energy calibration on some detectors requires identifying well-known emission lines. We envision a model that can be successfully trained without needing a highly accurate calibration approach. In this study, we used labeled data to train a neural network. In an experimental setting, this labeling technique might be possible by controlling experimental conditions. For example, the pulse fluence can be linked to transmission factors by attenuating the beam and placing proteins on a solid matrix (fixed target mode) [15] prior to an SFX experiment.

ACKNOWLEDGMENTS

The authors thank Jan-Erik Rubensson, Tomas André, and the Uppsala University Biophysics Network for insightful discussions. We thank Howard A. Scott for scientific mentorship and improvements to the collisional radiation code [38,39]. A.B., S.C., and N.T. acknowledge the Swedish Research Council (Grants No. 2019-03935 and No. 2023-03900) for financial support. H.A. and C.C. acknowledge the Center For Interdisciplinary Mathematics (CIM) at Uppsala University for financial support. C.C. acknowledges the Swedish Research Council (Grant No. 2018-00740), the Röntgen-Ångström Cluster (Grant No. 2019-03935), and the Helmholtz Association through the Center for Free-Electron Laser Science at DESY. All calculations were performed on the Davinci computer cluster provided by the Laboratory of Molecular Biophysics at Uppsala University.

All authors conceptualized the work; S.C. curated the data; S.C., H.A., and A.B. did the formal analysis, worked on the methodology, carried out the investigation and validation, and created the visualization; C.C. and N.T. acquired the funding and provided resources; S.C. administered the project; C.C. and N.T. supervised the work; S.C. and N.T. wrote the original draft; and all authors contributed to reviewing and editing.

DATA AVAILABILITY

The data that support the findings of this article are openly available [66].

[1] I. Schlichting and J. Miao, Emerging opportunities in structural biology with X-ray free-electron lasers, Curr. Opin. Struct. Biol. **22**, 613 (2012).

[2] J. C. H. Spence, XFELs for structure and dynamics in biology, IUCrJ **4**, 322 (2017).

[3] E. A. Seddon, J. A. Clarke, D. J. Dunning, C. Masciovecchio, C. J. Milne, F. Parmigiani, D. Rugg, J. C. H. Spence, N. R. Thompson, K. Ueda, S. M. Vinko, J. S. Wark, and W. Wurth, Short-wavelength free-electron laser sources and science: A review, Rep. Prog. Phys. **80**, 115901 (2017).

[4] T. R. M. Barends, B. Stauch, V. Cherezov, and I. Schlichting, Serial femtosecond crystallography, Nat. Rev. Methods Primers **2**, 59 (2022).

[5] I. Schlichting, Serial femtosecond crystallography: the first five years, IUCrJ **2**, 246 (2015).

[6] H. N. Chapman, C. Caleman, and N. Timneanu, Diffraction before destruction, Phil. Trans. R. Soc. B **369**, 20130313 (2014).

[7] C. Pellegrini, A. Marinelli, and S. Reiche, The physics of x-ray free-electron lasers, Rev. Mod. Phys. **88**, 015006 (2016).

[8] J. Grünert, M. P. Carbonell, F. Dietrich, T. Falk, W. Freund, A. Koch, N. Kujala, J. Laksman, J. Liu, T. Maltezopoulos, K. Tiedtke, U. F. Jastrow, A. Sorokin, E. Syresin, A. Grebentsov, and O. Brovko, X-ray photon diagnostics at the European XFEL, J. Synchrotron Radiat. **26**, 1422 (2019).

[9] T. Maltezopoulos, F. Dietrich, W. Freund, U. F. Jastrow, A. Koch, J. Laksman, J. Liu, M. Planas, A. A. Sorokin, K. Tiedtke, and J. Grünert, Operation of X-ray gas monitors at the European XFEL, J. Synchrotron Radiat. **26**, 1045 (2019).

[10] J. Grünert, W. Freund, J. Liu, T. Maltezopoulos, B. v. Kuiken, A. Scherz, Z. Konopkova, U. Zastrau, and T. Tanaka, Absolute photon power measurements at the European XFEL instruments, J. Phys.: Conf. Ser. **2380**, 012083 (2022).

[11] Y. Feng, J. M. Feldkamp, D. M. Fritz, M. Cammarata, R. Aymeric, C. Caronna, H. T. Lemke, D. Zhu, S. Lee, S. Boutet, G. Williams, K. Tono, M. Yabashi, and J. B. Hastings, A single-shot intensity-position monitor for hard x-ray FEL sources, in *X-Ray Lasers and Coherent X-ray Sources: Development and Applications IX*, Vol. 8140, edited by J. Dunn and A. Klisnick (SPIE/International Society for Optics and Photonics, San Diego, 2011), p. 81400Q.

[12] R. J. Bean, A. Aquila, L. Samoylova, and A. P. Mancuso, Design of the mirror optical systems for coherent diffractive imaging at the SPB/SFX instrument of the European XFEL, J. Opt. **18**, 074011 (2016).

[13] K. Ayyer *et al.*, 3D diffractive imaging of nanoparticle ensembles using an x-ray laser, Optica **8**, 15 (2021).

[14] K. Toyota, Z. Jurek, S.-K. Son, H. Fukuzawa, K. Ueda, N. Berrah, B. Rudek, D. Rolles, A. Rudenko, and R. Santra, *xcalib*: a focal spot calibrator for intense X-ray free-electron laser pulses based on the charge state distributions of light atoms, J. Synchrotron Radiat. **26**, 1017 (2019).

[15] A. Echelmeier, M. Sonker, and A. Ros, Microfluidic sample delivery for serial crystallography using XFELs, Anal. Bioanal. Chem. **411**, 6535 (2019).

[16] T. Gorkhover *et al.*, Nanoplasma dynamics of single large xenon clusters irradiated with superintense X-ray pulses from the linac coherent light source free-electron laser, Phys. Rev. Lett. **108**, 245005 (2012).

[17] P. Franz *et al.*, Terawatt-scale attosecond X-ray pulses from a cascaded superradiant free-electron laser, Nat. Photonics **18**, 698 (2024).

[18] P. J. Ho *et al.*, The role of transient resonances for ultra-fast imaging of single sucrose nanoclusters, Nat. Commun. **11**, 167 (2020).

[19] I. Inoue, J. Yamada, K. J. Kapcia, M. Stransky, V. Tkachenko, Z. Jurek, T. Inoue, T. Osaka, Y. Inubushi, A. Ito, Y. Tanaka, S. Matsuyama, K. Yamauchi, M. Yabashi, and B. Ziaja, Femtosecond reduction of atomic scattering factors triggered by intense x-ray pulse, Phys. Rev. Lett. **131**, 163201 (2023).

[20] C.-C. Kao, Challenges and opportunities for the next decade of XFELs, Nat. Rev. Phys. **2**, 340 (2020).

[21] A. Sanchez-Gonzalez *et al.*, Accurate prediction of X-ray pulse properties from a free-electron laser using machine learning, Nat. Commun. **8**, 15461 (2017).

[22] A. Hanuka, C. Emma, T. Maxwell, A. S. Fisher, B. Jacobson, M. J. Hogan, and Z. Huang, Accurate and confident prediction of electron beam longitudinal properties using spectral virtual diagnostics, Sci. Rep. **11**, 2945 (2021).

[23] K. Dingel, T. Otto, L. Marder, L. Funke, A. Held, S. Savio, A. Hans, G. Hartmann, D. Meier, J. Viefhaus, B. Sick, A. Ehresmann, M. Ilchen, and W. Helml, Artificial intelligence for online characterization of ultrashort X-ray free-electron laser pulses, Sci. Rep. **12**, 17809 (2022).

[24] N. Breckwoldt, S.-K. Son, T. Mazza, A. Rörig, R. Boll, M. Meyer, A. C. LaForge, D. Mishra, N. Berrah, and R. Santra, Machine-learning calibration of intense x-ray free-electron-laser pulses using Bayesian optimization, Phys. Rev. Res. **5**, 023114 (2023).

[25] D. E. Ferreira de Lima, A. Davtyan, J. Laksman, N. Gerasimova, T. Maltezopoulos, J. Liu, P. Schmidt, T. Michelat, T. Mazza, M. Meyer, J. Grünert, and L. Gelisio, Machine-learning-enhanced automatic spectral characterization of x-ray pulses from a free-electron laser, Commun. Phys. **7**, 400 (2024).

[26] K. K. Alaa El-Din, O. G. Alexander, L. J. Frasinski, F. Mintert, Z. Guo, J. Duris, Z. Zhang, D. B. Cesar, P. Franz, T. Driver, P. Walter, J. P. Cryan, A. Marinelli, J. P. Marangos, and R. Mukherjee, Efficient prediction of attosecond two-colour pulses from an X-ray free-electron laser with machine learning, Sci. Rep. **14**, 7267 (2024).

[27] T.-W. Ke, A. S. Brewster, S. X. Yu, D. Ushizima, C. Yang, and N. K. Sauter, A convolutional neural network-based screening tool for X-ray serial crystallography, J. Synchrotron Radiat. **25**, 655 (2018).

[28] Y. Sun and S. Brockhauser, Machine learning applied for spectra classification in x-ray free electron laser sciences, Data Sci. J. **21**, 15 (2022).

[29] J. Kern *et al.*, Simultaneous femtosecond x-ray spectroscopy and diffraction of photosystem II at room temperature, Science **340**, 491 (2013).

[30] T. Fransson, R. Chatterjee, F. D. Fuller, S. Gul, C. Weninger, D. Sokaras, T. Kroll, R. Alonso-Mori, U. Bergmann, J. Kern, V. K. Yachandra, and J. Yano, X-ray emission spectroscopy as an *in situ* diagnostic tool for X-ray crystallography of metalloproteins using an X-ray free-electron laser, Biochemistry **57**, 4629 (2018).

[31] B. Abraham, S. Nowak, C. Weninger, R. Armenta, J. Defever, D. Day, G. Carini, K. Nakahara, A. Gallo, S. Nelson, D. Nordlund, T. Kroll, M. S. Hunter, T. van Driel, D. Zhu, T.-C. Weng, R. Alonso-Mori, and D. Sokaras, A high-throughput energy-dispersive tender X-ray spectrometer for shot-to-shot sulfur measurements, a special issue on X-ray free-electron lasers., J. Synchrotron Radiat. **26**, 629 (2019).

[32] H.-J. Kunze, Diagnostic applications, in *Introduction to Plasma Spectroscopy*, edited by H.-J. Kunze (Springer, Berlin, Heidelberg, 2009), pp. 179–204.

[33] F. B. Rosmej, V. A. Astapenko, and V. S. Lisitsa, Applications to plasma spectroscopy, in *Plasma Atomic Physics*, edited by F. B. Rosmej, V. A. Astapenko, and V. S. Lisitsa (Springer International Publishing, Cham, 2021), pp. 459–592.

[34] W. Samek, G. Montavon, S. Lapuschkin, C. J. Anders, and K.-R. Müller, Explaining deep neural networks and beyond: A review of methods and applications, Proc. IEEE **109**, 247 (2021).

[35] L. Young *et al.*, Femtosecond electronic response of atoms to ultra-intense X-rays, Nature (London) **466**, 56 (2010).

[36] C. Caleman, G. Huldt, F. R. N. C. Maia, C. Ortiz, F. G. Parak, J. Hajdu, D. van der Spoel, H. N. Chapman, and N. Timneanu, On the feasibility of nanocrystal imaging using intense and ultrashort X-ray pulses, ACS Nano **5**, 139 (2011).

[37] K. Nass, Radiation damage in protein crystallography at X-ray free-electron lasers, Acta Crystallogr. D **75**, 211 (2019).

[38] H. A. Scott and R. W. Mayle, GLF - A simulation code for X-ray lasers, Appl. Phys. B **58**, 35 (1994).

[39] H. A. Scott, Cretin—a radiative transfer capability for laboratory plasmas, J. Quant. Spectrosc. Radiat. Transfer **71**, 689 (2001).

[40] S. Hansen, H.-K. Chung, C. Fontes, Y. Ralchenko, H. Scott, and E. Stambulchik, Review of the 10th non-LTE code comparison workshop, High Energy Density Phys. **35**, 100693 (2020).

[41] A. Barty *et al.*, Self-terminating diffraction gates femtosecond X-ray nanocrystallography measurements, Nat. Photonics **6**, 35 (2012).

[42] K. R. Beyerlein, H. O. Jönsson, R. Alonso-Mori, A. Aquila, S. Bajt, A. Barty, R. Bean, J. E. Koglin, M. Messerschmidt, D. Ragazzon, D. Sokaras, G. J. Williams, S. Hau-Riege, S. Boutet, H. N. Chapman, N. Tîmneanu, and C. Caleman, Ultrafast nonthermal heating of water initiated by an X-ray free-electron laser, Proc. Natl. Acad. Sci. USA **115**, 5652 (2018).

[43] I. Dawod, S. Cardoch, T. André, E. De Santis, J. E, A. P. Mancuso, C. Caleman, and N. Timneanu, MolDStruct: Modeling the dynamics and structure of matter exposed to ultrafast x-ray lasers with hybrid collisional-radiative/molecular dynamics, J. Chem. Phys. **160**, 184112 (2024).

[44] M. F. Gu, The flexible atomic code, Can. J. Phys. **86**, 675 (2008).

[45] J. Kubát, Statistical equilibrium equations for trace elements in stellar atmospheres, EAS Publ. Ser. **43**, 43 (2010).

[46] H. van Regemorter, Rate of collisional excitation in stellar atmospheres, Astrophys. J. **136**, 906 (1962).

[47] J. C. Stewart and K. D. Pyatt, Jr., Lowering of ionization potentials in plasmas, Astrophys. J. **144**, 1203 (1966).

[48] F. Chollet *et al.*, Keras (2015), https://github.com/fchollet/keras.

[49] T. O'Malley, E. Bursztein, J. Long, F. Chollet, H. Jin, L. Invernizzi *et al.*, keras-team/keras-tuner, https://github.com/keras-team/keras-tuner.

[50] M. Abadi *et al.*, TensorFlow: Large-scale machine learning on heterogeneous systems, 2015, software available from tensorflow.org.

[51] A. Shrikumar, P. Greenside, and A. Kundaje, Learning important features through propagating activation differences, in *Proceedings of the 34th International Conference on Machine Learning*, Proceedings of Machine Learning Research, edited by D. Precup and Y. W. Teh (PMLR, 2017), Vol. 70, pp. 3145–3153.

[52] S. M. Lundberg and S.-I. Lee, A unified approach to interpreting model predictions, in *Advances in Neural Information Processing Systems*, edited by I. Guyon, U. V. Luxburg, S. Bengio, H. Wallach, R. Fergus, S. Vishwanathan, and R. Garnett, Vol. 30 (Curran Associates, Inc., Red Hook, NY, 2017).

[53] R. Alonso Mori, E. Paris, G. Giuli, S. G. Eeckhout, M. Kavčič, M. Žitnik, K. Bučar, L. G. M. Pettersson, and P. Glatzel, Electronic structure of sulfur studied by X-ray absorption and emission spectroscopy, Anal. Chem. **81**, 6516 (2009).

[54] R. Deslattes, E. Kessler, P. Indelicato, L. d. Billy, E. Lindroth, J. Anton, J. Coursey, D. Schwab, J. Chang, R. Sukumar, K. Olsen, and R. Dragoset, X-ray transition energies database, 2005, https://dx.doi.org/10.18434/T4859Z.

[55] S. Poštić and M. Subašić, Extensive evaluation of image classifiers' interpretations, Neural Comput. Appl. **36**, 20787 (2024).

[56] R. Jenkins, R. Manne, R. Robin, and C. Senemaud, IUPAC—nomenclature system for x-ray spectroscopy, X-Ray Spectrom. **20**, 149 (1991).

[57] P. D. Pérez, A. C. Carreras, and J. C. Trincavelli, Structure of the sulfur K x-ray emission spectrum: influence of the oxidation state, J. Phys. B: At. Mol. Opt. Phys. **45**, 025004 (2012).

[58] A. A. Sorokin, S. V. Bobashev, T. Feigl, K. Tiedtke, H. Wabnitz, and M. Richter, Photoelectric effect at ultrahigh intensities, Phys. Rev. Lett. **99**, 213002 (2007).

[59] H. Fukuzawa *et al.*, Deep inner-shell multiphoton ionization by intense X-ray free-electron laser pulses, Phys. Rev. Lett. **110**, 173005 (2013).

[60] A. Rörig, S.-K. Son, T. Mazza, P. Schmidt, T. M. Baumann, B. Erk, M. Ilchen, J. Laksman, V. Music, S. Pathak, D. E. Rivas, D. Rolles, S. Serkez, S. Usenko, R. Santra, M. Meyer, and R. Boll, Multiple-core-hole resonance spectroscopy with ultraintense X-ray pulses, Nat. Commun. **14**, 5738 (2023).

[61] M. O. Krause and J. H. Oliver, Natural widths of atomic K and L levels, $K\alpha$ X-ray lines and several KLL Auger lines, J. Phys. Chem. Ref. Data **8**, 329 (1979).

[62] S.-K. Son, L. Young, and R. Santra, Impact of hollow-atom formation on coherent x-ray scattering at high intensity, Phys. Rev. A **83**, 033402 (2011).

[63] S.-K. Son, R. Boll, and R. Santra, Breakdown of frustrated absorption in x-ray sequential multiphoton ionization, Phys. Rev. Res. **2**, 023053 (2020).

[64] W. Błachucki, Y. Kayser, A. Wach, R. Fanselow, C. Milne, J. Sá, and J. Szlachetko, Resonant X-ray emission spectroscopy with a SASE beam, Appl. Sci. **11**, 8775 (2021).

[65] N. Rohringer and R. Santra, X-ray nonlinear optical processes using a self-amplified spontaneous emission free-electron laser, Phys. Rev. A **76**, 033416 (2007).

[66] H. Agelii, A. Bellisario, C. Caleman, N. Timneanu, and S. Cardoch, Data for "Predicting high-intensity femtosecond x-ray exposure on protein crystals with simulated x-ray emission spectra" [Data set], Zenodo (2025), doi:10.5281/zenodo.14973455.